REGISTRATION AND FUSION OF MULTIPLE IMAGES ACQUIRED WITH MEDIUM FORMAT CAMERAS

A.M. G. Tommaselli [a], M. Galo[a], J. Marcato Junior[a], R. S. Ruy[b], R. F. Lopes[a]

[a] Dept. of Cartography, Unesp - Univ Estadual Paulista, 19060-900 Pres. Prudente, SP, Brazil
{tomaseli, galo}@fct.unesp.br, {jrmarcato, eng.rodrigo.flopes}@gmail.com
[b] Engemap-Geoinformação, R. Stos Dumont, 160,19806-061, Assis, SP, Brazil, roberto@engemap.com.br

Commission I, WG V/I

KEY WORDS: Photogrammetry, Dual Head, camera calibration, fusion of multiple images.

ABSTRACT:

Recent developments in the technology of optical digital sensors made available digital cameras with medium format at favourable cost/benefit ratio. Many companies are using professional medium format cameras for mapping and general photogrammetric tasks. Image acquisition systems based on multi-head arrangement of digital cameras are attractive alternatives enabling larger imaging area when compared to a single frame camera. Also, acquisition of multispectral imagery is facilitated with the integration of independent cameras. Several manufactures are following this tendency, integrating individual cameras to produce high-resolution multispectral images. The paper will address the details of the steps of the proposed approach for system calibration, image rectification, registration and fusion. Experiments with real data using images both from a terrestrial calibration field and an experimental flight, will be presented. In these experiments two Fuji FinePix S3Pro RGB cameras were used. The experiments have shown that the images can be accurately rectified and registered with the proposed approach with residuals smaller than 1 pixel.

1. INTRODUCTION

Recent developments in the technology of optical digital sensors made available digital cameras with medium format at reasonable costs, when compared to high-end digital photogrammetric cameras. Due to this favourable cost/benefit ratio, many companies have adapted professional medium format cameras to be used in mapping and general photogrammetric tasks (Mostafa and Schwarz, 2000; Roig et al., 2006; Ruy et al., 2007; Petrie, 2009). Compared to classic photogrammetric film cameras (23x23cm format) or large format digital cameras, medium format digital cameras have smaller ground coverage area, although their resolution are also increasing (some models have sensors with 60 megapixels). Image acquisition systems based on multi-head arrangement of digital cameras are attractive alternatives enabling larger imaging area when compared to a single digital frame camera. Also, acquisition of multispectral imagery is facilitated when using independent cameras, although calibration should be made for each optical system. Mobile Mapping Units also use multiple camera mounts being necessary to fuse the acquired images accurately.

2. BACKGROUND

Several manufacturers are integrating individual cameras to produce high-resolution multispectral images. Independent developers are implementing their own low-cost systems with off-the-shelf frame cameras (Mostafa and Schwarz, 2000; Roig et al., 2006; Ruy et al., 2007; Petrie, 2009).

The simultaneously acquired images from the multiple heads can be processed as units (Mostafa and Schwarz, 2000) or they can be registered and mosaicked to generate a high resolution multispectral image (Doerstel et al., 2002). In any case, knowledge of the relative orientation between cameras is desirable.

One strategy is to directly measure the coordinates of the perspective center of each camera and to indirectly determine the orientation (rotation matrix) of these cameras using a bundle block adjustment (Doerstel et al., 2002). Another alternative is the simultaneous calibration of both Inner Orientation Parameters (IOP) and Relative Orientation Parameters (ROP) for two or more cameras using the constraints that the relative rotation matrix and the base distance, or base components, between the cameras heads are stable. The further constraint of an observed fixed distance between the external nodal points can also be included (Tommaselli et al, 2009).

Camera Calibration
Camera calibration aims to determine a set of IOP – Inner Orientation Parameters (usually, focal length, principal point coordinates and lens distortion coefficients) (Brown, 1971; Merchant, 1979, Clarke and Fryer, 1998). This process can be carried out using laboratory methods, such as goniometer or multicollimator, or stellar and field methods, such as mixed range field, convergent cameras and self-calibrating bundle adjustment. In the field methods, image observations of points or linear features from several images are used to indirectly estimate the IOP through bundle adjustment using the Least Squares Method. The mathematical model uses the colinearity equations and includes the lens distortion parameters (Equation 1).

$$F_1 = x_F - x_0 - \delta x_r + \delta x_d + \delta x_a + f \frac{m_{11}(X - X_0) + m_{12}(Y - Y_0) + m_{13}(Z - Z_0)}{m_{31}(X - X_0) + m_{32}(Y - Y_0) + m_{33}(Z - Z_0)} = 0 \quad (1)$$

$$F_2 = y_F - y_0 - \delta y_r + \delta y_d + \delta y_a + f \frac{m_{21}(X - X_0) + m_{22}(Y - Y_0) + m_{23}(Z - Z_0)}{m_{31}(X - X_0) + m_{32}(Y - Y_0) + m_{33}(Z - Z_0)} = 0$$

where x_F, y_F are the image coordinates and the X,Y,Z coordinates of the same point in the object space; m_{ij} are the rotation matrix elements; X_0, Y_0, Z_0 are the coordinates of the camera perspective center (PC); x_0, y_0 are the principal point coordinates; f is the camera focal length and δx_i δy_i are the effects of radial and decentering lens distortion (Brown, 1966) and the parameters of the affinity model (Habib and Morgan, 2003):

Using this method, the exterior orientation parameters (EOPs), inner orientation parameters (IOPs) and object coordinates of photogrammetric points are simultaneously estimated from image observations and using certain additional constraints. Self-calibrating bundle adjustment, which requires at least seven constraints to define the object reference frame, can also be used without any control points (Merchant, 1979; Clarke and Fryer, 1998). A linear dependence between some parameters arises when the camera inclination is near zero and when the flying height exhibits little variation. In these circumstances, the focal length (f) and flying height (Z–Z_0) are not separable and the system becomes singular or ill-conditioned. In addition to these correlations, the coordinates of the principal point are highly correlated with the perspective center coordinates (x_0 and X_0; y_0 and Y_0). To cope with these dependencies, several methods have been proposed, such as the mixed range method (Merchant, 1979) and the convergent camera method (Brown, 1971).

Multi-head camera calibration

Previous works on stereo or multi-head calibration usually involve a two-step calibration: in the first step, the IOPs are determined; in a second step, the EOPs of pairs are indirectly computed by bundle adjustment, and finally, the ROP are derived. Most of the existing methods do not take advantage of stability constraints (Zhuang, 1995; Doerstel et al., 2002).

Because the camera heads are tightly attached to an external mount in multi-camera systems, it can be assumed that the relative position and orientation of the cameras are stable during image acquisition. Therefore, certain additional constraints can be included in the bundle adjustment step. The inclusion of these constraints in the bundle adjustment seems reasonable because the estimation of relative orientation parameters (ROPs) from a previously adjusted block can result in significant deviations between different pairs of images, i.e., larger physical variations than expected, as have been observed in our practical experiments (see experiments section).

3. METHODOLOGY

Two multiple cameras systems were developed by the Photogrammetric Research Group at Unesp: The "System for Airborne Acquisition and Processing of Digital Images" (SAAPI) (Ruy et al., 2007) is a commercial project jointly developed with Engemap company and it was designed for single or dual camera arrangements (see Figure 1). For the dual arrangement, two Hasselblad digital cameras are positioned in a convergent configuration. The Armod (Automatic Reconstruction of Models) system is a lighter version, using two Fuji S3 Pro (13 megapixels cameras), and a Sony F828, which was adapted to acquire infrared images. The images are acquired simultaneously with a fixed superposition. Table 1 presents some technical data of both cameras.

Cameras	Fuji S3 Pro	SONY F828
Sensor	CCD – 23.0 x 15.5mm	CCD – 8.8 x 6.6 mm
Resolution	4256 x 2848 pels (12 MP)	3264 x 2448 pels (8 MP)
Pixel Size (mm)	0.0054	0.0027
Focal length (mm)	28.4	7.35

Table 1. Technical details of the cameras used in the Armod light system.

The approach proposed in this paper to generate larger images from dual head cameras follows four main steps: (1) dual head system calibration; (2) image rectification; (3) image registration and; (4) radiometric correction and fusion to generate a large image.
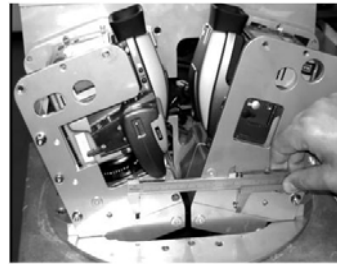

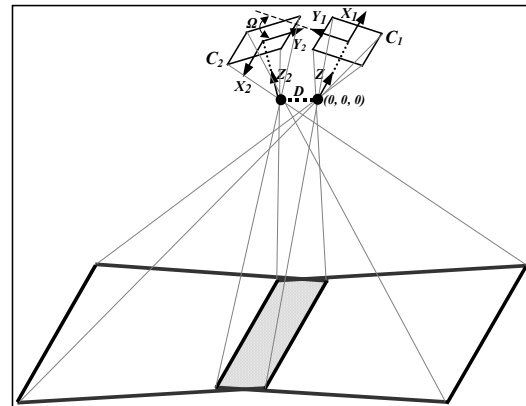Fig 1. Dual Head SAAPI system.

Fig 2. Armod light system.

Fig. 3. Geometry of a dual camera system.

The elements K, Φ and Ω are the RO angles referenced to the right camera (C1) and D is the Euclidian distance between C_1 and C_2. The approximated values of the angles Ω, Φ and K are -36º, 0º and 180º, respectively, for the SAAPI design, as shown in Figure 1 and 29º, 0º and 180º, respectively, for the Armod light version (Figure 2). The RO elements can be calculated as a function of the exterior orientation parameters (EOPs) of both cameras using Equation 2.

$$R_{RO} = R_1 (R_2)^{-1}, \qquad (2)$$

where R_{RO} is the RO matrix corresponding to the angles K, Φ, and Ω; R_1 and R_2 comprise the rotation matrix for cameras 1 and 2, respectively. The base distance D between cameras front nodal points can also be considered stable during acquisition. This distance can be directly measured because the location of the external nodal points can be obtained from the technical data provided by the camera and lens manufacturers and transferred to the external mount (Figure 1). This approach was already assessed but it was not used in the present experiments with the Armod system.

(1) Dual-head system calibration

The basic mathematical model for calibration of the dual-head system are the collinearity equations (Eq. 1) with additional

parameters and the constraints equations presented in this section (Tommaselli et al, 2009).

Let R_{RO}^t be the RO matrix and the squared distance between the cameras perspective centers, for the instant t and, analogously, for the instant $t+1$, R_{RO}^{t+1} and D_{t+1}^2. It is reasonable to consider the RO matrix and distance between the perspective centers stable, although the orientation of each camera changes. Based on these assumptions, the following equations can be written:

$$R_{RO}^t - R_{RO}^{t+1} = 0 \qquad (3)$$

$$D_t^2 - D_{t+1}^2 = 0 \qquad (4)$$

with:

$$R_{RO}^t = \begin{bmatrix} (r_{11}^1 r_{11}^2 + r_{12}^1 r_{12}^2 + r_{13}^1 r_{13}^2) & (r_{11}^1 r_{21}^2 + r_{12}^1 r_{22}^2 + r_{13}^1 r_{23}^2) & (r_{11}^1 r_{31}^2 + r_{12}^1 r_{32}^2 + r_{13}^1 r_{33}^2) \\ (r_{21}^1 r_{11}^2 + r_{22}^1 r_{12}^2 + r_{23}^1 r_{13}^2) & (r_{21}^1 r_{21}^2 + r_{22}^1 r_{22}^2 + r_{23}^1 r_{23}^2) & (r_{21}^1 r_{31}^2 + r_{22}^1 r_{32}^2 + r_{23}^1 r_{33}^2) \\ (r_{31}^1 r_{11}^2 + r_{32}^1 r_{12}^2 + r_{33}^1 r_{13}^2) & (r_{31}^1 r_{21}^2 + r_{32}^1 r_{22}^2 + r_{33}^1 r_{23}^2) & (r_{31}^1 r_{31}^2 + r_{32}^1 r_{32}^2 + r_{33}^1 r_{33}^2) \end{bmatrix}^{(t)}$$

where r_{ij} are the elements of rotation matrix for both cameras, with $i,j=\{1, 2, 3\}$.

Considering the Equations (3) and (4), based on the EOP for both cameras in consecutive instants (t and $t+1$), four constraints equations can be written:

$$G_1 = (r_{21}^1 r_{11}^2 + r_{22}^1 r_{12}^2 + r_{23}^1 r_{13}^2)^{(t)} - (r_{21}^1 r_{11}^2 + r_{22}^1 r_{12}^2 + r_{23}^1 r_{13}^2)^{(t+1)} = 0 \qquad (5)$$

$$G_2 = (r_{31}^1 r_{11}^2 + r_{32}^1 r_{12}^2 + r_{33}^1 r_{13}^2)^{(t)} - (r_{31}^1 r_{11}^2 + r_{32}^1 r_{12}^2 + r_{33}^1 r_{13}^2)^{(t+1)} = 0 \qquad (6)$$

$$G_3 = (r_{31}^1 r_{21}^2 + r_{32}^1 r_{22}^2 + r_{33}^1 r_{23}^2)^{(t)} - (r_{31}^1 r_{21}^2 + r_{32}^1 r_{22}^2 + r_{33}^1 r_{23}^2)^{(t+1)} = 0 \qquad (7)$$

$$G_4 = (X_0^{2(t)} - X_0^{1(t)})^2 + (Y_0^{2(t)} - Y_0^{1(t)})^2 + (Z_0^{2(t)} - Z_0^{1(t)})^2 -$$
$$(X_0^{2(t+1)} - X_0^{1(t+1)})^2 - (Y_0^{2(t+1)} - Y_0^{1(t+1)})^2 - (Z_0^{2(t+1)} - Z_0^{1(t+1)})^2 = 0 \qquad (8)$$

The mathematical models corresponding to the mentioned constraints were implemented using the C/C++ language on the CMC (Calibration of Multiple Cameras) program using the Least Squares combined model.

(2) Image rectification

The second step requires the rectification of the images with respect to a common reference system, using the EOP and the IOP computed in the calibration step.

The derivation of the EOP to be used for rectification was done empirically using the ground data calibration. From the existing pairs of EOP one was selected because the resulting fused image was near parallel to the calibration field. A rotation matrix with *common omega* and *common phi* angles was then computed to leave the resulting image plane parallel to the calibration field. This rotation matrix was applied to the EOPs of the selected image pair generating a set of EOPs for both cameras to be used in the rectification of all acquired images.

Rectification is performed by using collinearity equations (Eq. 1) with some particularities. Firstly, the dimensions and the corners of the rectified image are defined, by using the inverse collinearity equations. Then, the pixel size is defined and the relations of the rectified image with the tilted image are computed with the collinearity equations. The RGB values of

each pixel of the rectified image are interpolating in the projected position in the tilted image (See Fig. 4). The same procedure is applied for both images, but with different values for the projection planes, resulting in two RGB as shown if Fig. 5.
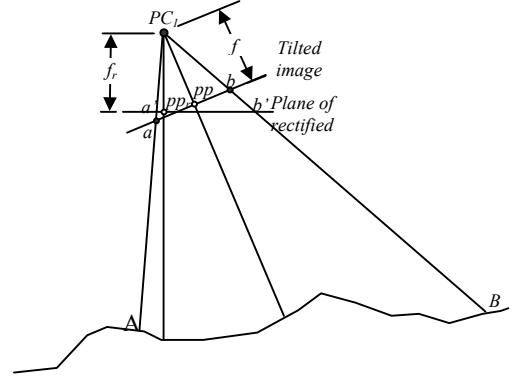

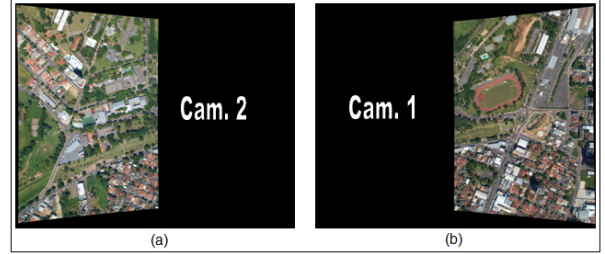Fig. 4 Geometry of image rectification.

Fig. 5. Resulting rectified images of dual cameras (a) left image is from camera 2 and, (b) right image is from camera 1.

In Figure 5 the resulting images encompass all the area of the original image. For practical reasons it can be better to crop the useful area as it is shown in Figure 6.

(3) Image registration

The third step is the registration of the rectified images using tie points located in the overlap area, for which some residual errors are detected. These points can be measured automatically with cross correlation functions or manually. The coordinates of these points should be the same, but can be slightly different, due to uncertainties in the EOPs and IOPs and also due to different PC positions. The discrepancies are assessed through the analysis of its standard deviations. In case the standard deviations are less than 2 pixels, the images can be fused.

(4) Images fusion

The fourth step is the images fusion, when large format multispectral images are generated (Fig. 6). Considering firstly the pairs of rectified RGB images, the average discrepancies of tie points in rows and columns are used to correct each pixel coordinates and then to assign the RGB values for the pixels of the final image. The average of differences in R, G and B values on the tie point areas in both images are used to compute a radiometric correction that is also applied to each pixel.

Several arrangements can be used, for example, two convergent RGB cameras, one RGB nadir camera and a second nadir IR camera or two convergent RGB cameras and one nadir IR camera.

The measurement of corresponding points between IR and RGB images cannot be done by using conventional area based correlation of grey levels due to the differences in spectral response in these wavelengths. Instead, in this work, a

correspondence method based on weighted correlation of gradients magnitudes and directions is introduced. The original IR image is resampled and rectified by using their calibrated EOPs. Then, some points are manually measured both in the reference RGB image and in the resampled IR image. These points are used to compute approximated polynomial parameters (Eq. 9) that will be used to define search areas. A grid is defined in the IR image and, in each neighbourhood of this grid points, interest points are located using Harris operator. These distinguishable points are then projected to the RGB image using the approximated polynomial coefficients and a correspondence function is evaluated for the neighbourhood of each point. This function compares the differences in gradients magnitude and directions in both images (RGB and IR) using an empirically defined weight for gradients and directions.

(a)

(b)
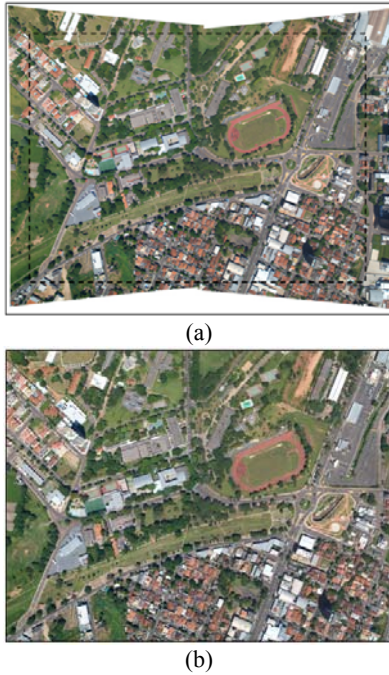
Fig. 6. Resulting fused image from two rectified images after registration (a) and, crop, eliminating the borders.

$$x' = a_0 + a_1 x'' + a_2 x''^2 + a_3 y'' + a_4 y''^2 + a_5 x'' y'' + a_6 x''^2 y''$$
$$y' = b_0 + b_1 x'' + b_2 x''^2 + b_3 y'' + b_4 y''^2 + b_5 x'' y'' + b_6 x''^2 y''$$, (09)

where a_i and b_i are the unknowns parameters, x'', y'' are coordinates in the IR image and x', y' are the coordinates of corresponding points in the RGB images.

4. EXPERIMENTAL ASSESSMENT

In these experiments two Fuji FinePix S3Pro RGB cameras and one Sony F828, adapted to acquire IR images, were used (See a picture of the camera system in Figure 2 and technical data in Table 1).

Firstly, the system was calibrated in a test field consisting of a wall with signalised targets. Several experiments were conducted to assess the results with distinct approaches and to check its effects in the rectified images. In these experiments, two Fuji S3 Pro with a nominal focal length of 28 mm were used. In the experiments, 32 images were used (16 for each camera) in four stations, resulting in 2008 image observations corresponding to circular targets in the test field (Figure 7). The image coordinates of circular targets were extracted with

subpixel accuracy using an interactive tool that computes the center of mass after automatic threshold estimation.

Four exposure stations were used, and in each station, eight images were captured (four for each camera), with the dual-mount rotated by 90º, -90º and 180º. After eliminating images with weak point distribution, 21 images were used: 11 images taken with camera 10 with camera 2; 6 images of camera 1 matched to corresponding images acquired with camera 2, with the result that 6 pairs were collected at the same instant. Figure 8 depicts some images acquired for the calibration step.
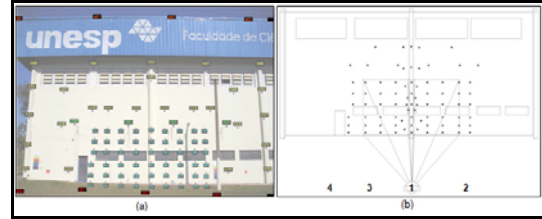

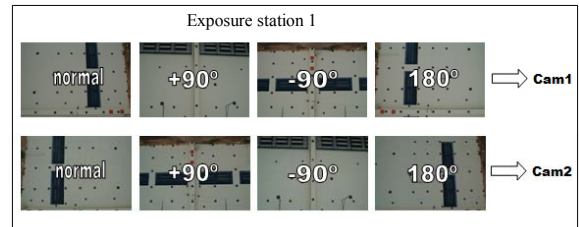Fig. 7 (a) Calibration field; (b) Targets location.

Fig. 8 Images acquired in the first exposure station.

Thus, from this group of 21 images, 6 pairs were taken at the same instant and the constraint equations can be written out accordingly. The group of 383 parameters estimated using Least Squares Estimation consists of: 6 EOPs for each image; 10 IOP for each camera; 3 coordinates for each point in the object space (81 total points). In this set of points, 51 were used as control points, 2 as check points and the remaining were considered photogrammetric (tie) points.

To assess the proposed methodology with real data, six experiments were carried out, without and with different weights for the RO constraints (Table 2). The experiments were carried out with RRMSC (Relative Rotation Matrix Stability Constraints – Equations 5 to 7) and BLSC (Base Length Stability Constraint), but varying the weights in the constraints. In the experiment A the two cameras were calibrated in two separated runs and in the experiment B the two cameras were calibrated in the same bundle system, but without RO constraints. In the experiments C to F, RO constraints were introduced with different weights, considering different variations admitted for the angular elements.

Exp.	RO Constraints	Variation admitted for RO angular elements	Variation admitted in camera base length
A	Single camera calibration	-	-
B	N	-	-
C	Y	1"	1 mm
D	Y	10"	1 mm
E	Y	15"	1 mm
F	Y	30"	1 mm

Table 2 Characteristics of the six experiments with real data.

For each experiment the average estimated standard deviations for the EOP were computed and they are shown in Figure 9.
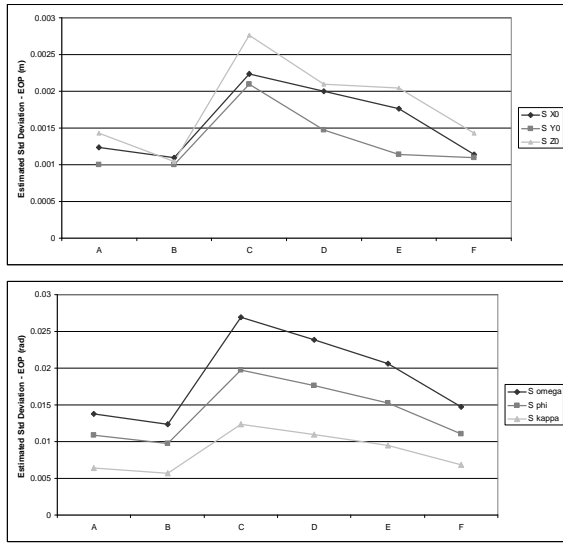

Fig. 9. Estimated standard deviations for the EOP.

In Figure 10 the estimated standard deviations for the IOP for both cameras are presented for each experiment. Also, in Figure 11 the a posteriori standard deviations for each experiment are presented.
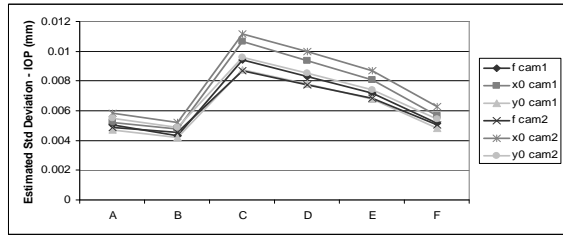

Fig. 10 Estimated standard deviations for the IOP for both cameras.

In Figure 12 the standard deviation of the discrepancies in the tie points between the rectified image pairs are presented. These deviations show the level of matching in the mosaicking of the dual images. It can be noted that augmenting the weight in the angular RO constraints produces smaller standard deviations for the IOP and EOP, but, on the other hand, the matching between the common areas of the rectified images is worse. This indicates that a good compromise is to admit a variation from 1" to 10" in the angular RO elements. The effects of varying the weight in the base constraint were not assessed in these experiments.
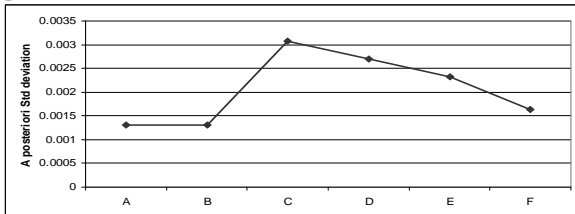

Fig. 11. A posteriori standard deviations for the experiments.

Figure 13 presents the RMSE of the discrepancies in the check points coordinates for all the experiments. Only two check points were used and it can be seen that the errors were slightly higher in the experiments with RO constraints. Imposing RO constraints enforces, in some extent, a solution that does not

adjust well for all the control points set, although the results in fusion of the image pairs are better.
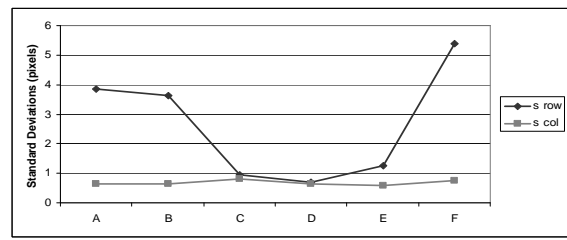

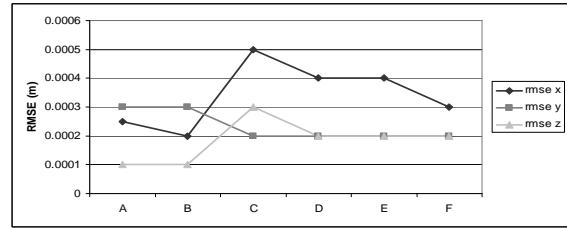Fig. 12. Standard deviations of the discrepancies in the tie points of the rectified image.

Fig. 13. RMSE of the discrepancies in the check points coordinates.

Table 3 show the values of some estimated IOP and their estimated standard deviations for the experiment D, in which constraints of RO stability showed the best results.

From the estimated EOP and ROP, common omega and phi rotations were empirically computed. These rotations were applied to the EOPs of both cameras in an exposure station that should produce an image plane parallel to the XY plane. These computed rotations were $\Phi c = 3.593^o$ and $\Omega c = 1.37^o$ and they were used to compute two sets of EOP, one for each camera (Table 4). Examples of images produced with these sets of parameters were shown in Figures 5 and 6.

Experiment	D	
IOP	CAMERA 1	CAMERA 2
f (mm) ±σ	28.5760 ± 0.0083(±1.54 pixel)	28.3709 ±0.0077 (± 1.43 pixel)
x₀ (mm) ±σ	0.2616 ±0.0093 mm (± 1.74 pixel)	-0.1040 ±0.0099 (±1.85 pixel)
y₀ (mm) ±σ	-0.0476 ±0.0078 (±1.44 pixel)	-0.2287 ±0.0085 (±1.58 pixel)

Table 3. Some IOPs for both cameras and their estimated standard deviation for experiment C.

The image fusion previously requires the computation of small translations in rows and columns and also radiometric adjustment. In the studied case a single radiometric translation for each band was enough. Translation in rows was –7 pixels and in columns –3 pixels. The radiometric translations in each channel (R, G and B) were ΔR = +15, ΔG= +15 and ΔB=+15. Figure 14 shows the cut line before and after the radiometric adjustment.

	ω (º)	φ (º)	κ (º)	X₀ (m)	Y₀ (m)	Z₀ (m)
Cam. 1	-0.451787	-14.508515	-89.731447	104.435	403.324	5.017
Cam. 2	0.393123	14.516444	90.128024	104.514	403.317	5.086

Table 4. EOP parameters recomputed to generate a virtual image near parallel to the XY plane.
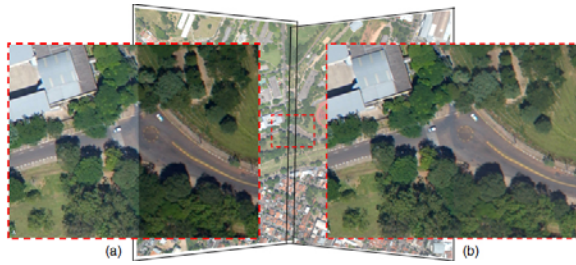
Fig. 14. Radiometric adjustment of the rectified pair: (a) before and (b) after the adjustment.
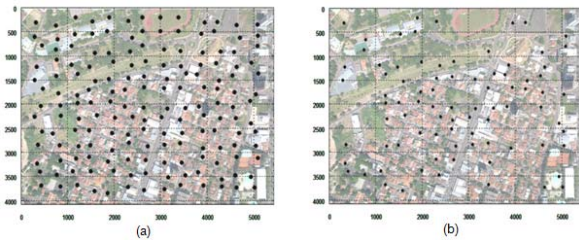

Fig. 15. (a) Interest Points automatically select by the Harris operator and (b) points used after residual analysis.

Fig. 15.a presents the interest points automatically selected by the Harris operators, whilst Fig. 15.b shows the points that were used to compute the final polynomial parameters. The original set of 169 distinguishable points was used to compute the polynomial parameters with Least Squares Methods. Points with residuals higher than 1.5 pixels were recursively eliminated, and 84 points were left (Fig. 15.b). The computed polynomial parameters with these 84 points were used to resample the IR and to produce an image presented in Fig. 16, where the G channel of the RGB image was replaced by the IR resampled image. The a posteriori sigma of the transformation was 0.7 pixels, which is an acceptable value, considering the resolution of the original IR image. Also, these matching results between two rectified oblique RGB images and one nadir IR image shows that the proposed methodology, with dual head calibration and subsequent rectification and fusion is successful.

Fig. 16 Color composition generated with the two rectified oblique RGB images and one nadir IR image after rectification and fusion.

5. CONCLUSIONS

In this paper a set of techniques for dual head camera calibration and images fusion were presented and experimentally assessed. Experiments were performed with Fuji FinePix S3Pro RGB cameras. The experiments have shown that the images can be accurately rectified and registered with the proposed approach with residuals smaller than 1 pixel, and they can be used for photogrammetric projects. Attention was paid to the calibration step, with a novel approach in which constraints considering the stability of Relative Orientation between cameras were applied to the bundle adjustment. The weights to be applied to the constraints are critical to reach acceptable image fusion.

6. REFERENCES

Brown, D.C., 1966. Decentering distortion of lenses, *Photogrammetric Engineering*, 32(3): 444-462.

Brown, D.C., 1971. Close-Range Camera Calibration, *Photogrammetric Engineering*, 37(8):855-866.

Clarke, T.A., and J.G. Fryer, 1998. The development of camera calibration methods and models*, Photogrammetric Record*, 16(91):51-66.

Doerstel, C., W. Zeitler, and K. Jacobsen, 2002. Geometric calibration of the DMC: method and results. *Proceedings of the ISPRS Commission I / Pecora 15 Conference*, Denver, International Archives for Photogrammetry and Remote Sensing (34)1, pp 324–333.

Habib, A., M. Morgan, 2003. Automatic calibration of low-cost digital cameras, *Optical Engineering,* 42(4): 948-955.

Merchant, D. C., 1979. *Analytical photogrammetry: theory and practice*. Notes Revised from Earlier Edition Printed in 1973, The Ohio State University, Ohio State.

Mostafa, M.M.R., and K.P. Schwarz, 2000. A Multi-Sensor System for Airborne Image Capture and Georeferencing. *Photogrammetric Engineering & Remote Sensing*, 66(12):1417-1423.

Petrie, G., 2009. Systematic Oblique Aerial Photography Using Multiple Digital Frame Camera, *Photogrammetric Engineering & Remote Sensing*, 75(2):102-107.

Roig, J., M. Wis, and I. Colomina, 2006. On the geometric potential of the NMC digital camera, *Proceedings of the International Calibration and Orientation Workshop – EuroCOW 2006,* 25-27 January, Castelldefels, Spain, unpaginated CDROM.

Ruy, R.S., A.M.G. Tommaselli, J.K. Hasegawa, M. Galo, N.N. Imai, and P.O. Camargo, 2007. SAAPI: a lightweight airborne image acquisition system: design and preliminary tests, *Proceedings of the 7th Geomatic Week – High resolution sensors and their applications*, 20-23 February, Barcelona, Spain, unpaginated CDROM.

Tommaselli, A. M.G., Galo, M., Bazan, W. S., Marcato Junior, J. Simultaneous calibration of multiple camera heads with fixed base constraint *In: Proceedings of the 6th International Symposium on Mobile Mapping Technology, 2009*, Presidente Prudente, 2009.

Zhuang, H., 1995. A self-calibration approach to extrinsic parameter estimation of stereo cameras. *Robotics and Autonomous Systems*, 15(3):189-197.